Sintering behavior and ionic conductivity of $Li_{1.5}Al_{0.5}Ti_{1.5}(PO_4)_3$ synthesized with different precursors

Dedicated to Professor Paul Heitjans on the Occasion of His 75th Birthday

Bambar Davaasuren[1*], Qianli Ma[1], Alexandra von der Heiden[1**], Frank Tietz[1,2***]

[1] Forschungszentrum Jülich GmbH, IEK-1: Materials Synthesis and Processing, D-52425 Jülich, Germany

[2] Forschungszentrum Jülich GmbH, IEK-12: Helmholtz-Institute Münster, D-52425 Jülich, Germany

* New address: King Abdullah University of Science and Technology, Core Labs and Research Infrastructure Central Office, Thuwal 23955-6900, Saudi Arabia

** New address: Forschungszentrum Jülich GmbH, Projektträger Jülich (PTJ-NMT), D-52425 Jülich, Germany

*** Corresponding author: f.tietz@fz-juelich.de

Abstract: $Li_{1.5}Al_{0.5}Ti_{1.5}(PO_4)_3$ (LATP) powders were prepared from different NO_x-free precursors using an aqueous-based solution-assisted solid-state reaction (SA-SSR). The sintering behavior, phase formation, microstructure and ionic conductivity of the powders were explored as a function of sintering temperature. The powders showed a relatively narrow temperature windows in which shrinkage occured. Relative densities of 95 % were reached upon heating between 900 °C and 960 °C. Depending on the morphological features of the primary particles, either homogeneous and intact microstructures with fine grains of about < 2 µm in size or a broad grain size distribution, micro-cracks and grain cleavages were obtained, indicating the instability of the microstructure. Consequently, the ceramics with a homogeneous microstructure possessed a much higher total ionic conductivity.

Keywords: densification, phase formation, microstructure, ionic conductivity, LATP

1 Introduction

NaSICON-type lithium aluminum titanium phosphate $Li_{1+x}Al_xTi_{2-x}(PO_4)_3$ (LATP) is one of the potential candidate electrolyte materials for all-solid-state batteries. In comparison to other lithium-ion conductors, LATP only contains elements that are abundantly available and the necessary starting materials for the synthesis of powder can be purchased in high quantities at low costs. Figure 1 shows the potential cost reduction with increasing packaging unit up to the 10 kg level. Further scaling effects can be expected towards the 100 kg or 1000 kg level. The absence of heavy elements like lanthanides, zirconium or niobium not only has a significant impact on the materials cost, but it also makes LATP a material with rather low density, which is beneficial for the final gravimetric energy density of an all-solid-state battery.

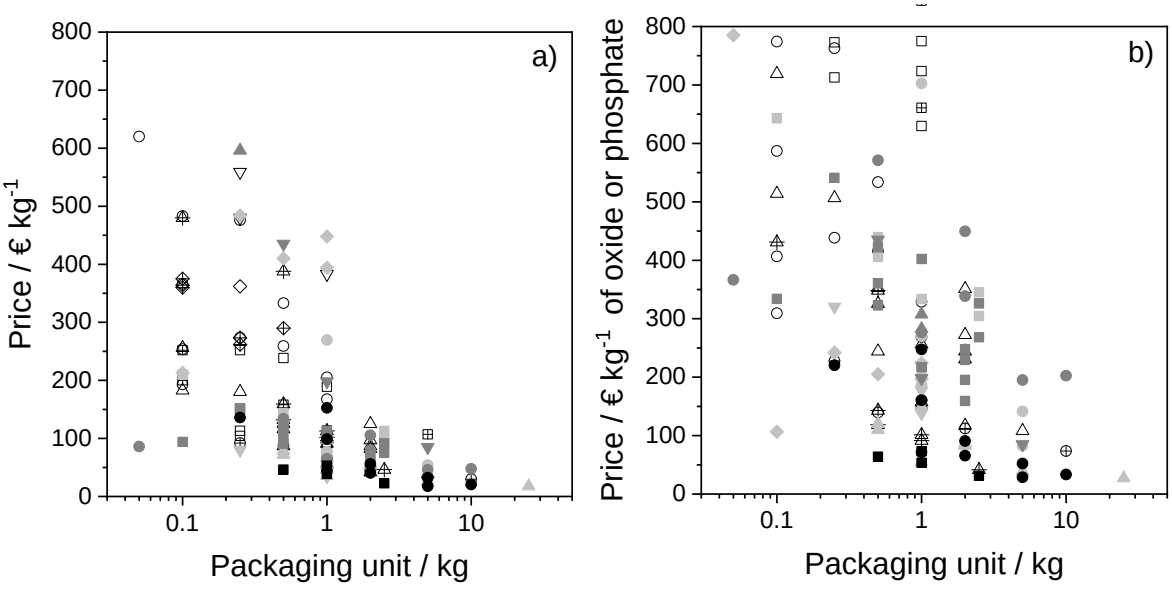

Fig. 1: Price of starting materials in relation to the packaging units for laboratory scale or pilot plant scale. a) Price of selected educts considering solubility in water, availability, ecological and toxic impact during synthesis: 9 lithium precursors (open and crossed symbols), 5 aluminum precursors (light gray symbols), 4 titanium precursors (dark gray symbols), 2 phosphate precursors (black symbols). b) Price of same precursors converted to effectively usable amount of oxide or phosphate.

In addition to the materials costs, the powder fabrication process is an important factor towards low-cost solid electrolytes influencing strongly the quality of the resulting ceramics [1]. Although it is common laboratory practice to use either highly soluble salts

like nitrates or organometallic compounds for sol-gel processing, e.g. [1-6], both approaches are unlikely to be transferred into industrial production. On the one hand the use of nitrates requires exhaust gas cleaning with ammonia to convert the nitrous fumes to nitrogen. The additional costs of this gas cleaning are not advantageous for industrial adaptation. On the other hand the precursors for sol-gel preparation are often very expensive even when purchased in large amounts. Therefore, the development of a purely inorganic sol [5] is a first step towards cost reduction and resulted in an LATP powder with excellent properties, but the use of nitrates remains as a main drawback.

At the other end of powder fabrication, i.e. at industrial level, the solid-state reaction method is often applied, because the raw materials (oxides, hydroxides, carbonates) are usually available at lower costs than other salts. However, the resulting powders are frequently coarse, very crystalline and have a low sinter ability. The quality of such powders can only be improved by high-energy milling to meet the powder quality that is necessary for the processing of solid-state batteries. The different qualities of the powders not only influence the processing of the ceramics, but also the intrinsic properties. As an example, solid-state nuclear magnetic resonance (NMR) measurements revealed significantly different short-range transport properties in LATP prepared by solid-state reaction and by sol-gel technique [7, 8] (Figure 2).

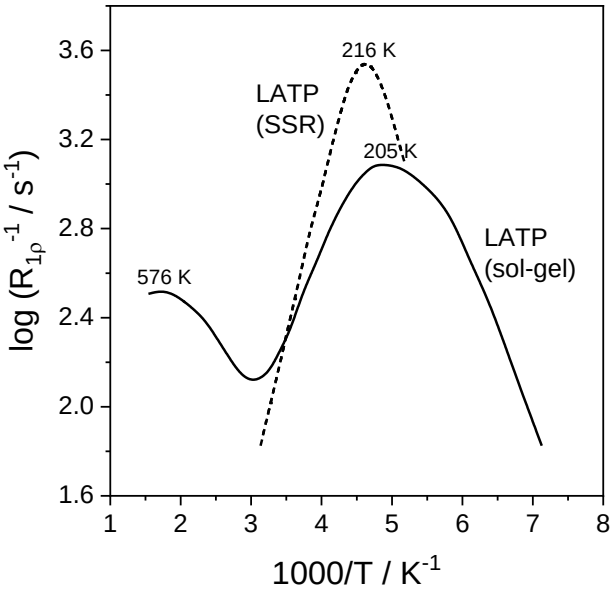

Fig. 2: Arrhenius plot of the ^{7}Li NMR spin-lattice relaxation rates $R_{1\rho}$ investigated in the rotating frame of $Li_{1.5}Al_{0.5}Ti_{1.5}(PO_4)_3$ prepared by sol-gel processing (solid line) [7] and by solid-state reaction (dashed line) [8].

As a compromise between sophisticated sol-gel preparation and the rather simple solid-state reaction method we have established the solution-assisted solid-state reaction (SA-SSR) method, which simplifies the sol-gel processing and tries to dissolve as much precursor in an aqueous solution as possible. First examples of this approach have already been reported showing promising powder qualities for the processing of highly conductive solid electrolytes [9-11]. The procedure is similar to the co-precipitation process described by Kotobuki et al. [12]. The SA-SSR takes into account economic, industrial and environmental aspects: low-cost materials, scalability, avoidance of additional chemicals like complexation agents, water as a solvent and utilization of NO_x-free precursor materials. Here, we report on the preparation of LATP using different NO_x-free precursors applying the SA-SSR method. The resulting powders were systematically examined for phase formation, microstructure, crystallinity and ion conductivity as a function of the sintering temperature.

2 Experimental

The SA-SSR route was developed for NASICON-type phosphate materials. The detailed experimental procedures were previously communicated and discussed for $Na_{3+x}Sc_xZr_{2-x}(SiO_4)_2(PO_4)$ [9], $Na_3Zr_2(SiO_4)_2(PO_4)$ [10] and $Li_{1.5}Al_{0.5}Ti_{1.5}(PO_4)_3$ [11]. In this work, five types of LATP powders were prepared using different precursor materials via the SA-SSR method. All the precursors were used as purchased. Table 1 summarizes the precursor combinations for the powder syntheses.

Table 1: Precursor materials for the different powder batches of $Li_{1.5}Al_{0.5}Ti_{1.5}(PO_4)_3$

Powder version	Li	Al	Ti	P
1	$LiOH \cdot H_2O$	$Al(CO_2CH_3)_2OH$	$Ti[OCH(CH_3)_2]_4$	$H_3(PO_4)$
2	$LiH_2(PO_4)$	$Al(CO_2CH_3)_2OH$	$Ti[OCH(CH_3)_2]_4$	$H_3(PO_4)$
3	$LiOH \cdot H_2O$	$Al(CO_2CH_3)_2OH$	TiO_2 –I *	$H_3(PO_4)$
4	$LiH_2(PO_4)$	$Al(CO_2CH_3)_2OH$	TiO_2 –II **	$H_3(PO_4)$
5	$LiOH \cdot H_2O$	$Al(H_2PO_4)_3$·	TiO_2 –II **	$H_3(PO_4)$

*: purchased from Alfa-Aesar (99.5%, 1-2 µm); ** purchased from Chempur (99 %, 0.2 µm)

The Al^{3+} precursor solution was prepared according to the published procedure using aluminum acetate basic hydrate $(CH_3COO)_2Al(OH) \cdot x\ H_2O$ (Alfa-Aeser) [11]. In general, all precursors were dissolved in water for the LATP powder synthesis or, as in the case of TiO_2, a slurry was formed. The water was subsequently evaporated from the solutions and the obtained solid mixture was calcined. The synthesis of powder version 2 (PV2) is described in more detail as an example. The details of the preparation of PV1 powder was reported in [11].

206.86 g LiH_2PO_4 (99 %, Sigma-Aldrich) was dissolved in deionized water for the synthesis of 1.314 mol (500 g) LATP. A stoichiometric amount of Al-acetate solution (885.86 g) was slowly added under continuous stirring. Afterwards, 227.19 g orthophosphoric acid H_3PO_4 (85 % Merck Chemicals) was loaded to the resulting transparent solution. The mixture was stirred for 20 minutes to ensure the homogeneity of the sample. Finally, 577.38 g titanium (IV) isopropoxide (97 % Sigma-Aldrich) was slowly added. The reaction mixture turned white and fine precipitates were formed. After stirring at room temperature for 4 h, the final reaction mixture was dried at 80 °C for 48 h. The dried solid was crushed and calcined at 600 °C for 5 h. The PV2 powder was obtained after ball milling on a rolling bench in ethanol for 48 h.

In the case of PV3 the dried reaction mixture was calcined at 350 °C, resulting in a very hard and dense mass. The specimen was crushed and milled in a planetary ball mill for 2 h. Afterwards, the resulting powder was calcined at 700 °C and ball-milled in ethanol to obtain the PV3 powder. After ball milling the suspension was probed with a laser scattering particle analyzer (Horiba LA-950V2) to determine the particle size distribution.

Inductively coupled plasma optical emission spectroscopy (ICP-OES) was utilized to quantitatively evaluate the stoichiometric composition of the calcined powders.

Differential thermal analysis/thermogravimetry (DTA/TG) measurements were carried out on the calcined powders up to 1000 °C in air with heating and cooling rates of 300 K/h using the simultaneous thermal analyzer STA449F1 Jupiter coupled to the QMS 403C Aëolos mass spectrometer from NETZSCH-Gerätebau GmbH.

The sintering behavior of the LATP powders was examined by dilatometry (DIL 402C, Netzsch) using cylindrical pellets 8 mm in diameter. Additionally, uniaxially pressed pellets (13 mm in diameter; 75 MPa pressure) were sintered in the temperature range from 650 °C to 960 °C with a dwell time of 5 h and a heating rate of 3 $K \cdot min^{-1}$. The density of the LATP ceramic was measured by the Archimedes' method using deionized and degassed water.

Powder X-ray diffraction (XRD) patterns were measured with a Bruker D4 diffractometer. The HighScore software suite [13] was used for phase analysis and X-ray diffraction pattern fitting.

Metallographic preparation of the sintered pellets was carried out using water-free cutting fluid (Struers Inc.) and 9 µm, 3 µm and 1 µm diamond suspensions (Cloeren Technology GmbH). The microstructural features of the polished pellets were analyzed with scanning electron microscopy (SEM; Merlin, Zeiss) after coating with a thin Pt layer to avoid charging effects.

For the impedance measurements, polished pellets were coated with Au on both sides and sealed in Swagelok cells inside an Ar-filled glovebox. The impedance spectra of the samples sintered at various temperatures were recorded in the low AC frequency range (7 MHz to 1 Hz, VMP-300; Bio-Logic SAS) and in the high frequency range (3 GHz to 1 MHz, E4991B Impedance Analyzer, Keysight).

The temperature-dependent impedance measurements between −30 °C and 80 °C were performed only for the samples sintered at high temperatures (900-960 °C). The impedance data were fitted by the ZView® software (Scribner Associates Inc.).

3 Results and discussion

3.1 Observations during calcination

In the case of PV4, and in contrast to PV3 as mentioned above, the substance after drying was a soft, sticky solid, which became softer during exposure to ambient air. This hygroscopic behavior led to strong difficulties in solidifying the reaction mixture. Calcination is intended to remove remaining water and organic components. In this case, however, the dried suspension of PV4 foamed very strongly during heat treatment and there were large yield losses due to reproducible frothovers. The influence of the temperature on the foaming of the suspension was investigated by means of a thermo-optical device (TOMMI plus, Fraunhofer ISC, Germany), which combines a high-temperature furnace with an optical dilatometer. The silhouette of the sample is recorded by a CMOS camera. Figure 3 shows single images of the thermo-optical measurement during the heating phase from 25 °C to 800 °C. On the basis of the individual images, it is evident that the raw powder strongly expanded up to approximately 150 °C. No further changes were observed at higher temperatures. As shown at the bottom of Figure 1, the calcined powder remained a hollow, brittle and very

porous hemisphere. Differential thermal analysis (DTA/TG) also showed that up to about 220 °C the major mass loss was caused by decomposed organic components and water (see supporting information, Figure S1). The same behavior was also observed with PV5. A possible explanation for this huge volume increase is the formation of a predominantly inorganic polymer layer composed of titania and phosphate groups, presumably supported by organic molecules on the titania surface and by absorbed water from the air. This layer was evidently very dense (gas-tight) initially and underwent plastic deformation at low temperatures due to the internal gas pressure in the initial state of the solid. The evaporation of water and residual organic compounds led to a large gas-filled cavity until first defects occurred in the outer layer. At this point, the plasticity of the layer was no longer given. The surface layer was so stiff that the solid did not collapse and remained as a hollow hemisphere. Due to this uncontrollable calcination behavior, PV4 and PV5 were not further considered in the following investigations.

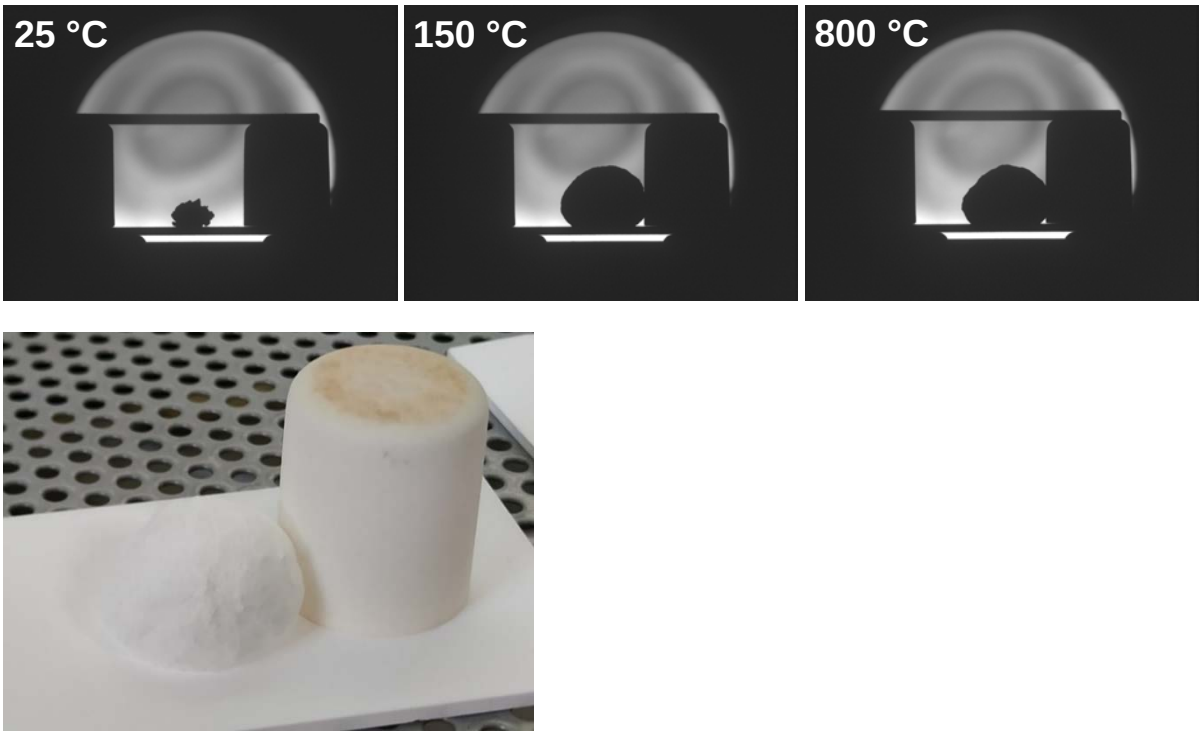

Fig. 3: Photographs of a thermo-optical measurement of the dried mass of PV4 from 25 °C to 800 °C. The silhouettes at 25 °C, 150 °C and 800 °C clearly show the large volume increase up to 150 °C. At the bottom, there is a photograph of the inflated ceramic body.

The reason for the very different behavior of the precursor mixtures used for PV3 and PV4 (PV5) can only be the different TiO_2 powders used in the three batches. Apart from

the different particle sizes (see footnote below Table 1), DTA/TG measurements revealed differences in weight losses up to 800 °C. Whereas the powder received from Alfa Aesar did not show any weight loss or DTA signal, the titania from Chempur lost about 0.72 % of its weight, 0.11 % between 90 and 220 °C and the remaining amount up to 550 °C. The simultaneously recorded data of the mass spectrometer gave clear evidence that the first weight loss was related to the release of water. The second weight loss, peaking at about 300 °C, was due to the combined evaporation of water and carbon dioxide. Obviously, the latter is a decomposition product of organic molecules that stabilizes the small particles of the TiO_2 powder against agglomeration. The small amount of organics in this powder was also apparently the reason for the formation of the plastic surface layer during the initial stages of the heat treatment of PV4 and PV5.

3.2 Powder characteristics and phase formation

The results of the ICP-OES analyses of the calcined powders are summarized in Table 2. All powders were of an acceptable quality in terms of stoichiometry compared to the nominal composition.

After ball milling, the calcined powders showed monomodal particle size distribution. For PV1, the particle size analysis showed a relatively broad distribution of particles with d_{50} = 5.73 µm due to less effective ball milling caused by remaining organics after calcination at 350 °C (Fig. 4a), while the morphology of the powder displayed an amorphous mass dominated by porous agglomerates. The PV2 and PV3 powders were obtained with relatively narrow particle size distributions with d_{50} of 0.78 µm and 0.83 µm, respectively. The primary particles of PV2 and PV3 were morphologically different. PV2 had spherical-shaped particles, whereas PV3 particles were block-shaped. Figures 4b and 4c show the SEM images of as calcined ball-milled PV2 and PV3 powders, respectively. The corresponding particle size distributions are displayed in Figure S2 of the Supporting Information (SI) together with the d_{50} values. It appears that the initial steps of powder processing may vary depending on the choice of starting materials.

The XRD patterns showed that the LATP with NaSICON structure was the majority phase already in the calcined powders. PV3 had sharp, well-defined peaks compared to PV1 and PV2 powders, which were related to the higher calcination temperature. The calcined powders contained different amounts of TiO_2, Li_3PO_4 and $AlPO_4$ as secondary phases (Figure S3a-c in SI). In addition, the amorphous mass in PV1 was responsible for a

broad hump at lower angles of the powder XRD pattern. The shape and width of the peaks indicate the fine grained nature of the crystalline phases in the three powders calcined between 350 °C and 700 °C.

Table 2: ICP-OES analysis results of the calcined LATP powders. The molar ratios are normalized to 3 mol phosphorus per formula unit.

Element	Nominal composition / mol	Analytical composition / mol (deviation / %)		
		PV1	PV2	PV3
Li	1.5	1.48 (-1.3)	1.46 (-2.4)	1.63 (9.0)
Al	0.5	0.48 (-4.4)	0.53 (5.9)	0.51 (2.2)
Ti	1.5	1.53 (2.0)	1.55 (3.4)	1.50 (0.2)
P	3	3	3	3

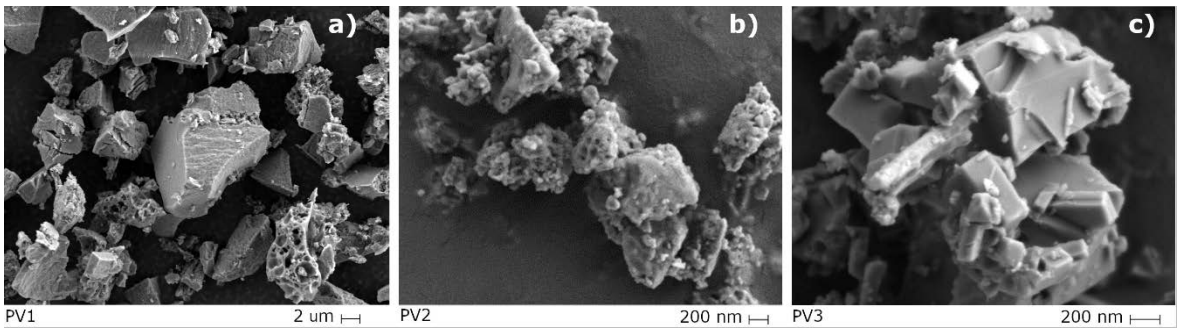

Fig. 4: SEM images of a) PV1 powder calcined at 350 °C, b) PV2 powder calcined at 600 °C and c) PV3 powder calcined at 700 °C.

It is interesting to note that the phase composition of the as-calcined powders varied depending on the precursor materials, which might be related to the varying phase equilibria under the given thermodynamic conditions. With increasing sintering temperature, the secondary phases slowly vanished and nearly-single-phase LATP was obtained at 850 °C, 960 °C and 900 °C for PV1, PV2 and PV3, respectively (Figure S3 and Figure 5c).

3.3 Sintering behavior, phase formation, densification and microstructure

Figure 5a displays the sintering behavior of the three powder variations during continuous heating in a dilatometer. The PV2 powder did not show sintering activity up to 825 °C, and then it shrank continuously until the end of the measurement. It reached 82 % of its original thickness after being heated to 960 °C and further shrank upon holding at 960 °C for 6 h. In contrast, PV1 and PV3 began to densify at around 750 °C and shrank up to 900 °C. To summarize, good quality ceramics with high densification (> 90 %) were obtained at 960 °C and 900 °C using PV2 and PV1 as well as PV3 powders, respectively. For further analysis, the powders were uniaxially pressed into 13 mm pellets and sintered at various temperatures with a heating and cooling rate of 180 $K \cdot h^{-1}$ and a dwell time of 6 h in a chamber furnace. The relative density of the sintered pellets was measured by the Archimedes' method using ethanol. The dependence of the relative density on the sintering temperature is shown in Figure 5b. The results are in excellent agreement with the dilatometry. PV2 did not densify up to 800 °C, as the relative densities of the pellets were similar to its green density of ~ 50 %. Starting from 850 °C the PV2 densified and reached about 95 % relative density at 960 °C. In the case of PV1, the densification increased linearly with sintering temperature, PV3 began to densify at 750 °C and at 850 °C the pellet already possessed 95 % relative density. It is important to note that the green density of PV3 was about 60 %, which is higher than for the two other powders.

Figure 5c shows the comparison of the XRD patterns of the powders after sintering at 900 °C for PV1 and PV3, and 960 °C for PV2, with the highest relative density amounting to 95 %. After sintering, PV1 and PV2 powders contain trace amounts of $AlPO_4$ and $LiTiOPO_4$, respectively, as a secondary phases. The PV3 also contained very small amount of an unidentified impurity (e.g. small reflection at about $2\Theta \approx 23°$) at the highest temperature of the thermal treatments. The presence of different impurity phases might be related to the starting materials, which may lead to different reaction routes to yield the LATP product. The unit cell parameters of three powders were obtained by indexing the powder XRD patterns and are in agreement with the values reported in the literature (Table 3): PV1 a = 8.4869(5) Å, c = 20.777(6) Å; PV2 a = 8.4935(2) Å, c = 20.7750(5) Å and PV3 a = 8.4914(2) Å, c = 20.7722(5) Å.

The microstructural features of the pellets sintered at various temperatures were investigated. The pellets were broken and a piece was taken for metallographic preparation. The cross-sectional SEM images of the PV2 and PV3 samples sintered at different temperatures are shown in Figure S4 and S5 and can be compared with the images taken from PV1 in [12]. The SEM results confirm the dilatometry and relative

density measurements. At lower sintering temperatures the microstructure consisted of fine particles/agglomerates. At 850 °C, the particles of PV2 began to coalesce to form small grains. The PV2 pellet sintered at 900 °C possessed a very homogeneous grain size distribution with about 75 % relative density (Figure 5e). After heating at 960 °C, a well-densified ceramic was formed with 95 % relative density (Figure S4). The microstructure featured homogeneous grain size distribution with grain sizes < 2 µm. The PV1 and PV3 powders had very similar microstructural features. Both sets of pellets shrank from 800 °C and highly dense ceramics had already formed at 850 °C. The PV1/PV3 pellets sintered above 900 °C had inhomogeneous grain growth (Figures 5d and 5f). Apart from this, grain cleavages and micro-cracks were observed. These microstructural observations are typical for agglomerated powders [14]. Like other triphosphates with NaSICON-structure, LATP showed thermal expansion anisotropy due to its symmetry ($R\bar{3}c$) and very different expansion of the lattice parameters *a* and *c* in hexagonal setting [15-19] (Table 3), which led to micro-cracks and deterioration of total ionic conductivity [20]. It was demonstrated that micro-cracking was clearly related to the grain size [4, 18, 21] and the critical grain size for micro-cracking of LATP was estimated to be ≤ 1.6 µm [21, 22]. Using the data in Table 3 and the empirically determined "master curve" for the critical grain size as a function of the inverse of the $(\alpha_a - \alpha_c)^2$ values [21], a critical grain size of about 1.5 µm was derived for LATP and 0.8-0.85 µm for $LiTi_2P_3O_{12}$. Therefore, it seems that the microstructure of PV2 is more stable against micro-cracking than the

Table 3: Crystallographic lattice parameters at room temperature and thermal expansion coefficients (α, all values in 10^{-6} K^{-1}) of $Li_{1+x}Al_xTi_{2-x}P_3O_{12}$

Compound	*a* / Å	*c* / Å	α_a	α_c	$\alpha_a - \alpha_c$	α_{XRD}*	Ref.
$LiTi_2P_3O_{12}$	8.5117	20.8524	0.49	30.8	30.31	10.47	[15]
$LiTi_2P_3O_{12}$	8.5115	20.8554	-0.05	30.6	30.65	10.16	[16]
$Li_{1.3}Al_{0.3}Ti_{1.7}P_3O_{12}$	8.500	20.820	0.43	31.8	31.37	10.89	[17]
$Li_{1.3}Al_{0.3}Ti_{1.7}P_3O_{12}$	-	-	0.38	31.0	30.62	10.59	[18]
$Li_{1.3}Al_{0.3}Ti_{1.7}P_3O_{12}$	8.5064	20.8325	0.03	23.06	23.03	7.71	[19]
$Li_{1.4}Al_{0.4}Ti_{1.6}P_3O_{12}$	8.4955	20.8017	2.02	26.87	24.85	10.30	[19]
$Li_{1.5}Al_{0.5}Ti_{1.5}P_3O_{12}$	8.4941	20.7921	0.39	23.02	22.63	7.93	[19]

*: $\alpha_{XRD} = 1/3\ \alpha_c + 2/3\ \alpha_a$

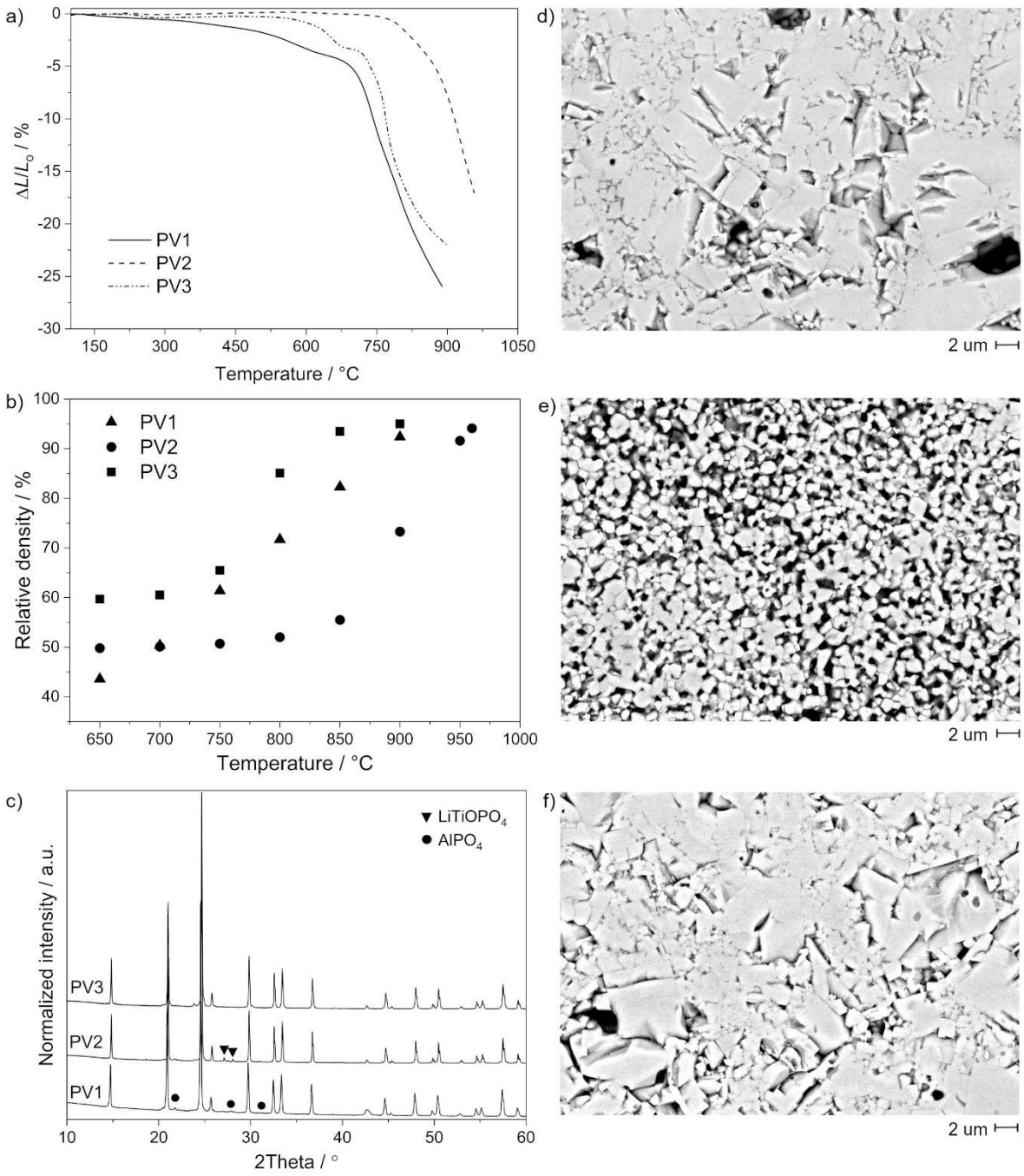

Fig. 5: a) Sintering behavior of PV1, PV2 and PV3 powders, b) relative density of the pellets sintered at various temperatures, c) powder XRD patterns of sintered PV1, PV2 and PV3 powders at 900-960°C, d), e) and f) SEM images of polished cross-sections of the PV1, PV2 and PV3 pellets sintered at 900 °C, respectively.

microstructures of PV1 and PV3. Consequently, better ionic transport properties are expected of PV2 samples. The microstructural difference between the three powders was most probably related to the shape of the primary particles. During the drying step, the

PV1 and PV3 powders formed bigger agglomerates. It should be noted that the LATP has a very narrow temperature window for shrinkage. Therefore, the processing of dense ceramics with homogeneous grain size distribution may require fine tuning and optimization of the particle size, shape, calcination and sintering temperature, as well as heating and dwelling time.

3.4 Ionic conductivity

The ionic conductivity of the sintered pellets was measured using impedance spectroscopy. The bulk and total ionic conductivity was calculated using the resistance value obtained after fitting the impedance spectra. The low frequency impedance spectra displayed only one semicircle and a straight line in the kHz-Hz region at room temperature, which was fitted with two circuits consisting of a resistance in parallel to a constant phase element (R-CPE). Using the fitting parameters, the capacitance value of the semicircle was calculated. The capacitance values were in the range of 10^{-10}-10^{-8} F and the semicircle was unambiguously assigned to grain boundary resistance [10,11, 23]. As expected, the grain boundary resistance of the three types of pellets decreased with increasing sintering temperature. The Nyquist plots of the samples sintered at various temperatures are shown exemplarily for PV2 in Figure 6a (for the Nyquist plots of PV1 and PV3 samples please refer to [11] and Figure S6, respectively). The relative density-dependent total ionic conductivity, measured at 25 °C, is shown in Figure 6b. For all three powders, the total ionic conductivity exponentially increased with increasing density of the sample, i.e. with increasing sintering temperature. It is interesting to observe that the total ionic conductivity of the PV2 powder was higher than that of PV1 and PV3 at all relative densities above 55%. PV2 showed highest the total ionic conductivity of 0.67 $mS \cdot cm^{-1}$ for the sample sintered at 960 °C, while PV1 and PV3 had the highest conductivity of 0.58 $mS \cdot cm^{-1}$ and 0.21 $mS \cdot cm^{-1}$, respectively, for the samples sintered at 900 °C. These values are in the same range as previously reported values for LATP [1-6, 15-19, 24, 25]. Other reports dealing with the impact of varying precursor materials [12, 26] also showed a similar scatter of the conductivity values. Presumably the microstructural features discussed above are the key parameter for the total resistance of the ceramics. This would explain why the homogenous grain size distribution of PV2 resulted in a higher ionic conductivity of the samples.

The bulk ionic conductivity of LATP was detected by applying high-frequency impedance spectroscopy in the region of 3 GHz to 1 MHz. For all three powder variants the bulk ionic conductivity also varied with the sintering temperature [11] (Figures 6c, 6d

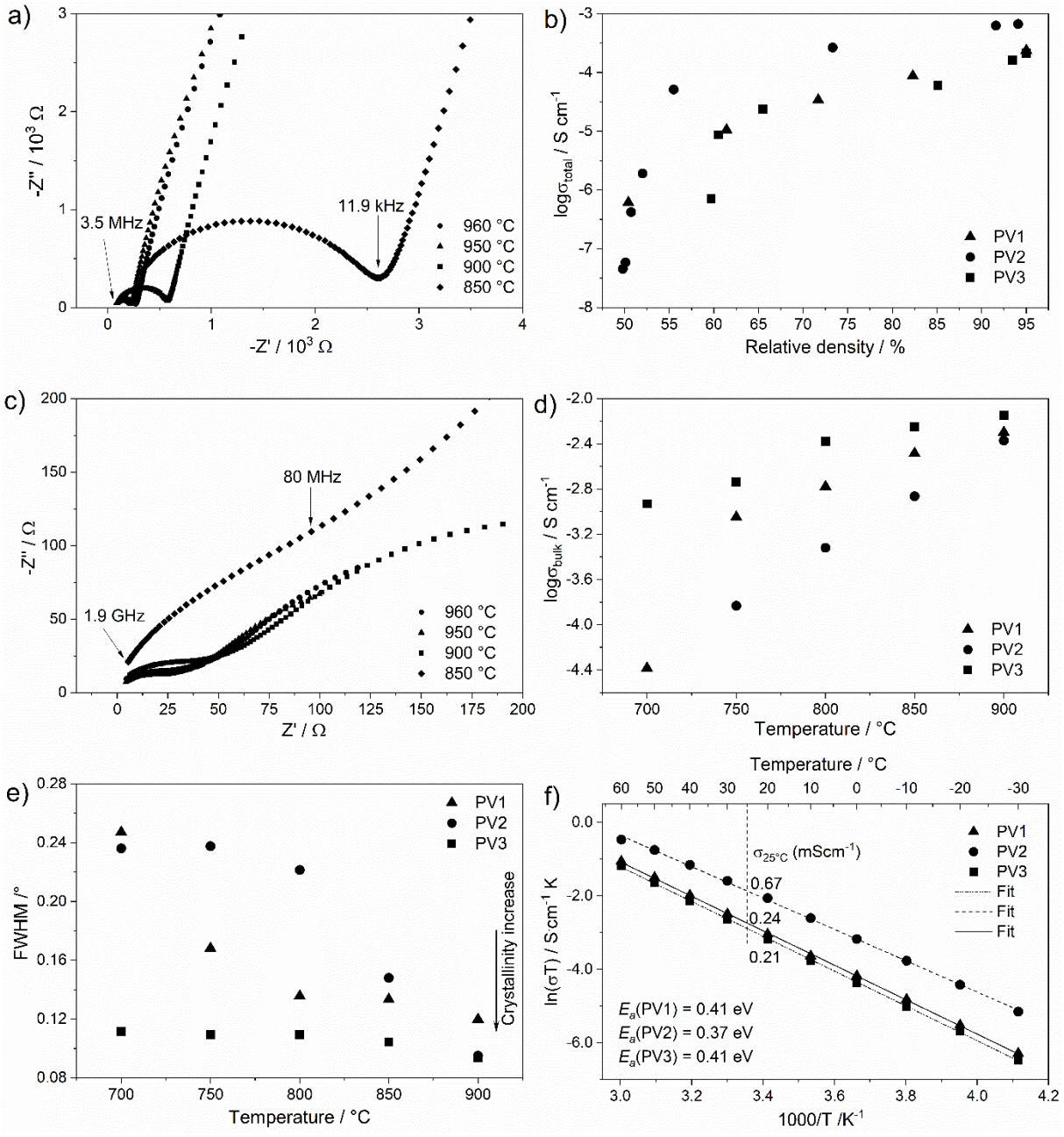

Fig. 6: a) Impedance spectra of PV2 pellets measured in the low frequency range, b) total ionic conductivity at 25 °C of PV1, PV2 and PV3 pellets as a function of relative density, c) impedance spectra of PV2 pellets measured in the high frequency range, d) bulk ionic conductivity of PV1, PV2 and PV3 pellets as a function of sintering temperature, e) FWHM of the (102) reflection as a function of sintering temperature and f) Arrhenius plot of PV1, PV2 and PV3 after sintering at 900 °C, 960 °C and 900 °C, respectively.

and S7). The bulk conductivity value obtained for PV3 was higher than that of PV1 and PV2, which is associated with the crystallinity. The bulk ionic conductivity of the samples was calculated and correlated with the crystallinity of the ceramics at the given sintering temperature. The (102) X-ray diffraction peak was selected for profile fitting and the full width at half maximum (FWHM) of the peak was taken as a measure for crystallinity. Figure 6e shows the dependence of the crystallinity (in terms of FWHM) on the sintering temperature. As mentioned before, PV3 had a higher degree of long-range order compared to PV1 and PV2 at all temperatures.

In the next step, temperature-dependent impedance studies were carried out. The temperature-dependent impedance measurements allowed the activation energy of the ionic transport to be calculated using the Arrhenius expression $\sigma T = A \cdot exp(-\frac{E_a}{kT})$ where σ is the ionic conductivity of the sample, A is the pre-exponential factor, κ is the Boltzmann constant and T is the absolute temperature. Figure 6f shows the Arrhenius plot of PV1, PV2 and PV3 after sintering at 900 °C, 960 °C and 900 °C, respectively, measured between -30 °C to 60 °C. The activation energy, E_a, was obtained from the linear fit of the experimental data. The E_a value for PV2 was 0.37 eV, which is comparable to the values reported in the literature [1-6, 12, 15-19, 24-26]. The E_a of PV3 was 0.41 eV, which is exactly the same as the E_a of PV1. This again clearly shows the importance of the microstructural parameters for the ionic transport in ceramic materials.

The activation energy for bulk ionic conductivity was determined in same manner, in the temperature range of -30 to 60 °C (Figure S8). It seems that the temperature-dependent bulk ionic conductivity data can be fitted using two temperature regimes, ranging from 60 °C to 20 °C (ΔT1) and from 10 °C to -30 °C (ΔT2) for both PV2 and PV3. This data might indicate that the diffusion of the Li^+ ions follow different mechanisms depending on the temperature range. The bulk E_a of the PV2 and PV3 powders determined in the range ΔT1 was 0.14 eV and 0.16 eV, respectively. The data fitted for ΔT2 gave E_a values of 0.30 eV and 0.26 eV for PV2 and PV3, respectively. In the case of PV1, the temperature-dependent impedance could be reliably fitted only from 40 °C to -30 °C. The data allowed a single linear fitting for PV1 powder in this temperature region and the E_a determined for the transport in the LATP lattice of PV1 was 0.27 eV. These E_a values determined for the migration of Li^+-ion within the LATP lattice are in excellent agreement with those obtained from ^7Li spin lattice relaxation measurements (0.16-0.17 eV [7], 0.29 eV) [8]) and those from DFT calculations (0.19 eV) [27].

Conclusions

The commercially available precursors for the synthesis of LATP were selected on the basis of the following six criteria: solubility, price per kilogram, price per kilogram oxide, availability, ecological considerations and health hazards. Good quality LATP can be synthesized on a kg-scale by SA-SSR using various precursors fulfilling the above-mentioned criteria. The synthesis of LATP by SA-SSR can be easily scaled up. Depending on the precursor material, the processing steps, i.e. the powder conditioning methods, and phase formation may vary. An example is the PV3 powder, which required additional grinding and high-energy ball milling steps. The homogeneous grain size distribution led to a high ionic conductivity of the ceramic. It seems that i) selection of proper precursor material; ii) control of particle size and shape; iii) avoiding the agglomeration of particles during powder preparation; and iv) optimization of calcination and sintering temperatures are the key parameters to obtain homogeneous grain size distribution and stable microstructure and consequently superior ionic conductivity.

Acknowledgements: We thank Dr. D. Grüner (FZJ, IEK-2) for the SEM investigations, M. Andreas and V. Bader for technical assistance, and A. Hilgers for PSD and M.-T. Gerhards for DTA/TG and dilatometry measurements. We also thank our colleagues at the Central Institute of Engineering, Electronics and Analytics (ZEA-3) for the ICP-OES analysis.

The results of this work are part of the project "BCT – Battery Cell Technology" funded by the German Federal Ministry of Education and Research (BMBF) under support code 03XP0109E. The authors take responsibility for the content of this publication.

References

1. Zhao E., Ma F., Jin Y., Kanamura K., *J. Alloys Comp.* 2016, *680*, 646-653
2. Kunshina G. B., Gromov O. G., Lokshin E. P., Kalinnikov V. T., *Russ. J. Inorg. Chem.* 2014, *59*, 424-430
3. Xu X., Wen Z., Wu J., Yang J., *Solid State Ionics* 2007, *178*, 29-34
4. Bucharsky E.C., Schell K.G., Hintennach A., Hoffmann M.J., *Solid State Ionics* 2015, *274*, 77-82
5. Ma Q., Xu Q., Tsai C.-L., Tietz F., Guillon O., *J. Am. Ceram. Soc.* 2016, *99*, 410-414
6. Key B., Schroeder D. J., Ingram B. J., Vaughey J. T., *Chem. Mater.* 2012, *24*, 287-293

7. Epp V., Ma Q., Tietz F., Wilkening M., *Phys. Chem. Chem. Phys.* 2015, *17*, 32115-32121
8. Vinod Chandran C., Pristat S., Witt E., Tietz F., Heitjans P., *J. Phys. Chem. C* 2016, *120*, 8 436-8442
9. Ma Q., Guin M., Naqash S., Tsai C.-L., Tietz F., Guillon O., Chem. Mater. 2016, 28, 4821-4828
10. Naqash S., Ma Q., Tietz F., Guillon O., *Solid State Ionics* 2017, *302*, 83-91
11. Davaasuren B., Tietz F., *Solid State Ionics* 2019, *338*, 144-152
12. Kotobuki M., Kobayashi B., Koishi M., Mizushima T., Kakuta N., *Mater. Technol. A* 2014, *29*, A93-A97
13. Degen T., Sadki M., Bron E., König U., Nénert G., *Powder Diffr.* 2014, *29*, S13-S18
14. Hallopeau L., Bregiroux D., Rousse G., Portehault D., Stevens P., Toussaint G., Laberty-Robert C., *J. Power Sources* 2018, *378*, 48-52
15. Woodcock D. A., Lightfoot P., *J. Mater. Chem.* 1999, *9*, 2907-2911
16. Huang C. Y., Agrawal D. K., McKinstry H. A., *J. Mater. Sci.* 1995, *30*, 3509-3514
17. Prasada Rao R., Maohua C., Adams S., *J. Solid State Electrochem.* 2012, *16*, 3349-3354
18. Hupfer T., Bucharsky E. C., Schell K. G., Senyshyn A., Monchak M., Hoffmann M. J., Ehrenberg H., *Solid State Ionics* 2016, *288*, 235-239
19. Case D., McSloy A. J., Sharpe R., Yeadel S. R., Bartlett T., Cookson J., Dashjav E., Tietz F., Kumar C. M. N., Goddard P., *Solid State Ionics* 2020, *346*, 115192
20. Oota T., Yamai I., *J. Am. Ceram. Soc.* 1986, *69*, 1-6
21. Yamai I., Ota T., *J. Am. Ceram. Soc.* 1993, *76*, 487-491
22. Jackman S. D., Cutler R. A., *J. Power Sources* 2012, *218* ,65-72
23. Sinclair D. C., *Bol. Soc. Esp. Cerám. Vidrio* 1995, *34*, 55-65
24. Kotobuki M., Koishi M., Kato Y., *Ionics* 2013, *19*, 1945-1948
25. Rossbach A., Tietz F., Grieshammer S., *J. Power Sources* 2018, *391*, 1-9 and references therein
26. Kotobuki M., Koishi M., *Ceram. Int.* 2013, *39*, 4645-4649
27. Lang B., Ziebarth B., Elsässer C., *Chem. Mater.* 2015, *27*, 5040-5048